Microstructure development of pearlitic railway steels subjected to fast heating

Mattos Ferreira, V.; Mecozzi, M. G.; Petrov, R. H.; Sietsma, J.

DOI
10.1016/j.matdes.2022.110989

Publication date
2022

Document Version
Final published version

Published in
Materials and Design

Materials & Design 221 (2022) 110989

Contents lists available at ScienceDirect

Materials & Design

journal homepage: www.elsevier.com/locate/matdes

Microstructure development of pearlitic railway steels subjected to fast heating

V. Mattos Ferreira [a], M.G. Mecozzi [a], R.H. Petrov [a,b], J. Sietsma [a]

[a] Delft University of Technology, Department of Materials Science and Engineering, Mekelweg 2, 2628 CD Delft, the Netherlands
[b] Ghent University, Department of Electrical Energy, Metals, Mechanical Constructions and Systems, Technologiepark 903, Ghent, Belgium

HIGHLIGHTS

- Comparable hardness is obtained for WEL produced in laboratory and the one from field conditions.
- Similar microstructural features are observed between WEL from field and after a single cycle of fast heating and quenching.
- Grain refinement observed in WEL produced during wheel/rail contact is not reproducible by thermal heating only.
- Mn homogeneization is obtained after 5 minutes soaking at high temperatures.

GRAPHICAL ABSTRACT

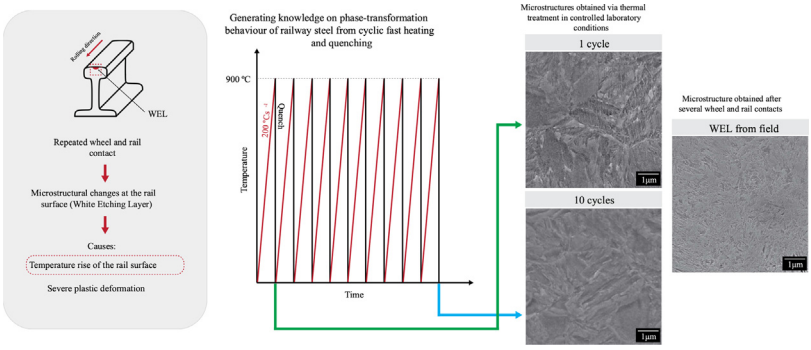

ARTICLE INFO

Article history:
Received 9 May 2022
Revised 8 July 2022
Accepted 23 July 2022
Available online 2 August 2022

Keywords:
Rails
White etching layer
Phase transformation
Fast heating

ABSTRACT

The influence of soaking and cooling rates on the final microstructure of a R260Mn pearlitic railway steel subjected to fast heating is investigated. Fast-heating experiments followed or not by soaking and cooling at different rates were performed using quenching dilatometry on railway steel specimens obtained from the rail head. Additional cyclic heating and quenching experiments were done to investigate the evolution of the microstructure during thermal cycling, which is relevant for railway applications. The final microstructure is characterized via microhardness measurements, optical microscopy and scanning electron microscopy. The microstructural features are distinguished and the influence of each condition is detailed. The study allows the construction of transformation diagrams during cooling after fast heating. Furthermore, comparison between the final microstructures obtained in controlled laboratory conditions and field White Etching Layers is presented. The obtained results can serve as a guideline for future reproduction of White Etching Layers in laboratory conditions and interpretation of field conditions.

1. Introduction

Since many years, railway transportation has been one of the main forms of passengers and freight transportation around the world. The main advantages of this type of transportation lie in its ability of handling large passenger and freight flows, low cost and congestion-free traffic. Besides that, its carbon emission is lower than other types of inland transportation, especially when combined with clean energy sources. This makes it attractive to many global societies which face a constant growth of urban areas and are constantly searching for cleaner transportation alternatives. Therefore, investments in railway infrastructure and services are important for more sustainable communities.

A key component of the railway infrastructure is the steel railway track, which requires regular maintenance and track replacement. Unexpected maintenance leads to undesirable traffic

https://doi.org/10.1016/j.matdes.2022.110989
0264-1275/

interruptions which decreases the reliability of the system and leads to additional costs. For the past years, researchers have been investigating different aspects of railway systems such as steel microstructure, contact loadings and failure mechanisms [1–5]. Their aim was to understand the complex phenomena that occur during rail/wheel contact. Although these studies have led to great findings, the comprehension of these mechanisms is still incomplete.

It is known that railway tracks are subjected to two main damage mechanisms: rolling contact fatigue and wear [6,7]. These mechanisms cause degradation of the rail geometry profile as well as deterioration of the material properties. For the past years, many studies have focused on understanding the microstructural essence of damage development in railway tracks. It was found that repeated wheel/rail contacts induce microstructural changes at the rail surface [8–10]. Two different layers have been observed at the rail surface: White Etching Layer (WEL) and Brown Etching Layer (BEL), named due to their white and brownish contrast in optical microscope after etching with 2% Nital (2% HNO_3 in ethanol). These layers are associated with preferential sites for crack nucleation and propagation due to their brittle nature and to the interface with the pearlitic base material. For this reason, more insight into the mechanism which leads to microstructural evolution at the surface of rails is necessary for its prevention and consequent increase of the rails service life and safety.

There are two main theories which were suggested to explain the formation of WEL and BEL. The first theory suggests that these layers are formed due to severe plastic deformation which induces cementite dissolution and grain refinement at the railway surface [11,12]. In this case the layers are considered to be composed of carbon-supersaturated nanocrystalline ferrite. The second theory proposes that these layers are actually formed as a consequence of cyclic ultrafast heating of the surface during wheel passage [13,14]. The temperature should in this explanation be high enough to promote the austenitization of those regions which will be followed by fast cooling, forming a nanocrystalline martensitic structure. Evidence for the second theory lies on the fact that retained austenite and small fractions of cementite can be observed in such layers which can only occur if at least partial austenitization takes place [15,16]. Additionally, computer simulations have confirmed the possibility of surface heating above austenitization temperature during wheel and rail contact [17–19]. However, some researchers are hesitant to accept that the surface can be heated to high temperatures of around 800 °C or more in milliseconds during wheel/rail contact. Although these two hypotheses were suggested, none is fully accepted.

Reproducing the exact loading conditions as on the actual railway in a laboratory is not possible at the moment. Also, the formation of these layers in field takes place in many cycles and these types of experiments are not possible. An attempt of measuring the temperature rise during wheel contact could be an option but currently existing devices are not able to detect such rise of temperature in milliseconds at the location where wheel/rail contact occurs. This makes it harder to reach agreement on which theory is more realistic. As the exact conditions are not reproducible, a good approach is to understand the behavior of railway steel when subjected to fast heating, which is the main goal of the present paper.

This paper focuses on the microstructural evolution of a commonly used railway steel grade (R260Mn) when subjected to several heat treatments with fast heating. This allows for a comparison of the microstructural characteristics of field-formed layers with those simulated under controlled laboratory conditions.

Additionally, the present study aims at providing insight into the behavior of the present steel grade to serve as guideline for understanding WEL and BEL formation. In order to do this, samples from an actual railway track were subjected to fast heating at 200 $°Cs^{-1}$ up to 900 °C. Although in practice heating rates may be higher, using this heating rate provides understanding of the phase transformation behaviour of R260Mn steel grade when subjected to fast heating. After heating, two routes were applied: (a) soaking for 5 min at 900 °C prior to cooling with different cooling rates or (b) cooling immediately after reaching 900 °C with different cooling rates.

The soaking allows the understanding of the influence of prior-austenite grain structure and homogenization of carbon in the final microstructure formed, which can also take place during repeated wheel passages in in-field railway steel. As railway steels undergo multiple cycles while in operation, another experiment was conducted to better understand the impact of cyclic heating and cooling on the behaviour of these steels. For this, a sample was subjected to 10 cycles of fast heating and quenching, without soaking at high temperature. Instead of precisely replicating the wheel and rail circumstances, the main objective of the cycling experiment is to gain information of its effect on the phase transformation behaviour of railway steels.

The first part of this paper focuses on the microstructural features found for each testing condition. As a consequence, a Continuous Cooling Transformation (CCT) diagram for R260Mn railway steels subjected to rapid heating was created. In the second part, the effect of cyclic heating on the microstructural aspects of the rails is presented along with a comparison to a WEL formed after repeated cycles of wheel/rail contact in field conditions. The combination of these findings can be used as a reference for steel manufacturers and researchers interested in reproducing WEL and BEL in laboratory conditions and better understanding of field circumstances.

2. Material and Methods

2.1. Material

The material selected for this study is the R260Mn railway steel grade provided by DekraRail, Utrecht, the Netherlands. The chemical composition of the as-received material is shown in Table 1. The initial microstructure consists of pearlite (89% ferrite and 11% cementite) with average hardness and interlamellar spacing of 292 HV and 150 nm, respectively, see Fig. 1. The material also contains 1.7% of pro-eutectoid ferrite decorating the prior-austenite grain boundaries. Furthermore, X-ray Diffraction analysis did not detect the presence of retained austenite in the as-received material.

The equilibrium transformation temperature range of austenite formation was calculated using the software Thermo-Calc. Fig. 2 shows the mole fractions of the phases in equilibrium as a function of temperature for R260Mn steel. These calculations provide insight into the annealing temperature for dilatometry measurements. It can be seen that the austenitic transformation is complete at a temperature (A_3) equal to 730 °C.

2.2. Methods

A DIL805 Bähr Dilatometer was used to perform fast heating and cooling in R260Mn steel. Dilatometry allows tracking of phase transformations by measuring the change in length of the specimen throughout the heat treatment. In this study, flat dilatometry samples with 10 mm length, 4 mm width and 1.5 mm thickness were cut from the rail head of the R260Mn steel with the length coinciding with the running direction of the rails. Two thermocouples were used in order to keep track of possible temperature gra-

Table 1
Chemical composition (in wt.%) of as-received R260Mn steel.

Element	C	Mn	Si	Cr	P	S	V
wt.%	0.64	1.40	0.29	0.03	0.01	0.01	0.001

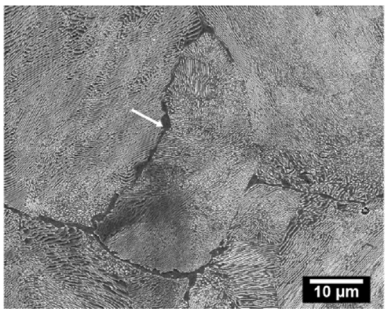

Fig. 1. Scanning electron microscopy image of the as-received R260Mn railway steel evidencing the pearlitic microstructure with the white arrow indicating pro-eutectoid ferrite at the grain boundaries.

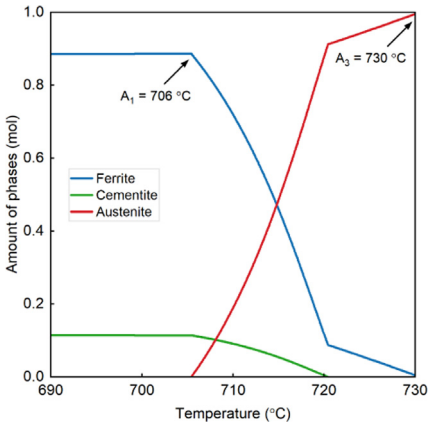

Fig. 2. Equilibrium transformation diagram of R260Mn steel calculated with Thermo-Calc software.

dients which can affect the final result interpretation. These thermocouples have been welded to the specimen's surface at the middle (TC1) and edge (TC2) of its length.

In order to achieve a fully austenitic microstructure that will transform into martensite during fast cooling, the annealing temperature must be above the A_3 temperature as calculated by Thermo-Calc software. For this reason the chosen annealing temperature for all heat treatments was 900 °C. This temperature is distinctly higher than the equilibrium value, which accounts for shifts in A_1 and A_3 temperatures due to ultrafast heating.

A graphical representation of the heat treatments is depicted in Fig. 3. Each specimen was heated at 200 °Cs^{-1} up to 900 °C. The specimens were then cooled at different controlled cooling rates (0.1, 1, 10 °Cs^{-1}) and quenched, either directly after heating (D) or after soaking at 900 °C for 5 min (S). The 5 min soaking at high temperatures allows austenite grain growth and possible element homogenization in austenite. As a result, the effect of different initial austenite conditions on the phase transformation and final microstructure can be investigated. Helium atmosphere was used during cooling in all experiments except for those with cooling rate 0.1 °Cs^{-1}, which were cooled under vacuum. The specimen identification has been done in the following manner: A_z with A being the type of heat treatment (D or S) and z the cooling rate value

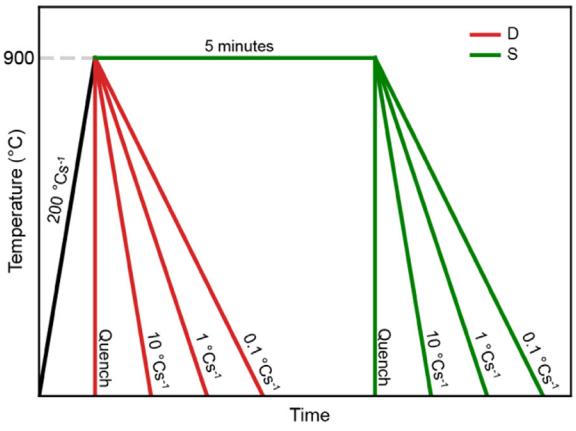

Fig. 3. Graphical representation detailing the heat treatments performed using dilatometry. Heat treatments D consist of fast heating at 200 ° Cs^{-1} up to 900 ° C and direct cooling with different cooling rates. Heat treatments S account for the same fast heating stage followed by intermediate soaking for 5 min at 900 ° C before cooling with different cooling rates.

(0.1, 1, 10 or quench). In addition, a cyclic heat treatment was performed aiming at understanding the response of the studied material when subjected to thermal cycling. For these experiments, the samples were heated with 200 ° Cs^{-1} up to 900 °C and immediately quenched for a total of ten cycles.

After the heat treatment, dilation curves were plotted and the fractions of transformation products formed were calculated using the lever rule with respect to BCC and FCC linear expansion curves following the method described in Ref. [20]. The retained austenite fractions obtained via XRD measurements were used to calibrate the BCC expansion curves in terms of the phase fractions. The determination of the transformation-start temperatures was done by detecting the temperature at which approximately 2% of newly-formed structural constituent is obtained. After being subjected to its respective heat treatment, the surface of the samples at which the thermocouples were welded was ground and polished up to 1 μm diamond paste using standard metallographic techniques. X-ray diffraction (XRD) was carried out in a Bruker D8 Discover diffractometer with a Eiger-2 500 k 2D-detector to obtain the phase fractions at room temperature. The 2θ scan was performed using Cu-Kα radiation in the angular range from 30° to 150° 2θ and a step size of 0.040° 2θ. Vickers microhardness measurements were done on the as-polished samples using a Durascan 70 (Struers) hardness tester by applying a load of 0.1 kgf for 10 s. The procedure was followed by etching with Nital 2% for 10 s to reveal the microstructures, which were observed in a Keyence VHX 6000 light optical microscope. Higher magnification micrographs were obtained with a JEOL JSM-6500F scanning electron microscope using a 15 kV accelerating voltage, 10 mm working distance and secondary electron imaging detection mode. Electron Probe Micro Analysis (EPMA) was performed with a JEOL JXA 8900R microprobe using an electron beam with energy of 10 keV and beam current of 100 nA employing Wavelength Dispersive Spectrometry (WDS). The points of analysis were located along two 500 μm long lines with points 2 μm apart and involved the elements C, Si, Cr and Mn determining the Fe concentration by difference.

3. Results and Discussion

3.1. Heating

Fig. 4a shows the dilatometry curves obtained during the heating stage of the heat treatment for each specimen analysed in this work. As only austenite formation took place during heating, the graph is enlarged in this area for a detailed analysis. Oscillations were present prior to austenite formation for many samples, due to the difficulty of the equipment to adjust the power input during very fast heating. In order to overcome this, the control parameters of the dilatometer equipment have been adjusted to obtain a smoother curve as for specimen D_{10}, highlighted in black. As the oscillations did not affect the heating profiles which showed high reproducibility, the specimens were still considered valid in this work. The dilatometry curves presented in Fig. 4a allow to extract information regarding the kinetics and the temperature range for austenite formation.

The experimental results presented in Fig. 4a show that a deviation from linearity starts at approximately 736° C. Since austenite has a more compact lattice than ferrite and cementite, a contraction is expected to occur during pearlite to austenite transformation, leading to a decrease of the change in length versus temperature. However, an expansion instead of a contraction is observed at the beginning of the austenitic transformation, followed by the expected contraction. Interrupted heating experiments were performed up to 751 ° C to understand whether austenite forms at the onset of the expansion. As can be seen in the inset of Fig. 4a, small fractions of martensite (austenite at high temperatures) are formed at temperatures up to 751 ° C, confirming that austenite nucleates at the very start of the peak.

The same expansion peak before austenite formation is observed in the sample subjected to cyclic heating and quenching. Fig. 4b presents the heating dilatometry curves obtained for each cycle. A clear distinction between the first (black line) and the following cycles is noted. The first cycle is characterized by an expansion of the sample with a maximum at 775 °C during pearlite to austenite transformation. When the sample is reheated in the second cycle, fluctuations are observed in the dilatometry curve between 200 and 500 °C, which are due to tempering of the martensite formed at the end of the first cycle after quenching. During tempering, carbide precipitation is expected to occur, reducing the carbon content of martensite which leads to a slight contraction of the sample [21]. At approximately 735 °C, the austenite starts nucleating and growing in the tempered martensite. In this case, however, the magnitude of the expansion peak during the martensite to austenite transformation is substantially smaller than for pearlitic initial microstructure. The actual A_{c1} and A_{c3} acquired from dilatometry curves for a heating rate of 200 °Cs^{-1} are 736 °C and 825 °C, respectively. These values are higher than the equilibrium A_1 and A_3 calculated by Thermo-Calc, see Fig. 2, since the experiments were conducted in non-equilibrium conditions with a heating rate of 200 °Cs^{-1}. Finally, all experiments were carried out up to 900 °C which guarantees complete austenitization.

Additional investigation was done to understand the nature of the dilatation peak observed for all samples. Fig. 4c shows the temperatures (TC1 and TC2) and power supply necessary to maintain the heating rate at 200 °Cs^{-1} as a function of time for the first heating stage of the D_{cyclic} sample. It is important to note that the power is adjusted according to the temperature profile registered at TC1 (middle of the sample). A sharp increase of the power is required to maintain the desired heating rate when TC1 records a temperature equal to 757 °C (Fig. 4c). This temperature corresponds to the Curie Temperature (T_{Curie}) of ferrite in pearlite, calculated based on the Mn content of ferrite (0.5 at.%) [14]. Since at this point the edge of the sample (TC2) is at about 60 °C below this temperature, the sharp increase of the power causes a rise of the heating rate in this still ferromagnetic region, with a consequent increase of the dilatation signal. T_{Curie} in this case is similar to the start of austenite formation, approximately 751 °C.

In the subsequent cycles, however, the initial microstructure is tempered martensite instead of pearlite. The martensitic structure is assumed to have the same overall Mn content as the alloy composition (2 at.%) which leads to a decrease of T_{Curie} to approximately 735 °C. In this case, the start of austenite formation occurs after crossing T_{Curie} and a two-step increase of power is observed with a less pronounced dilatation peak, Fig. 4b. For this reason, it can be concluded that the dilation peak is related with the gradient temperature of the sample which is evidently due to the fast heating imposed.

3.2. Prior-austenite grain size

It is known that high-temperature soaking and cyclic thermal treatments can alter the prior-austenite grain (PAG) structure [22–24] and, as a result, the final microstructure. For this reason, an investigation of the PAG structure is needed in order to understand the microstructures after the heat treatment. In this section, the EBSD scans obtained for samples subjected to slow cooling (0.1

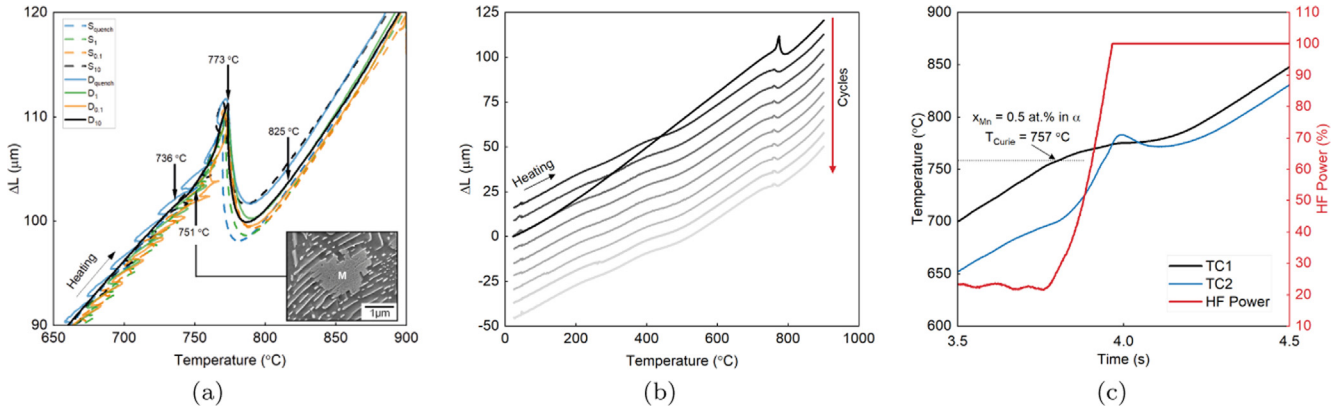

Fig. 4. (a) Heating stage of dilatometry curves for all specimens analysed in this work with focus on the intercritical temperature range where austenite formation takes place. Additionally, the SEM micrograph shows small patches of martensite (austenite at high temperatures) growing in the pearlitic matrix when sample was heated up to 751 °C followed by quench. (b) Heating stages of sample D_{cyclic} with increasing order of the cycles is indicated with a red arrow. (c) Temperature and HF Power as a function of time for the first heating cycle of D_{cyclic}.

°Cs^{-1} and 1 °Cs^{-1}), fast cooling (quench) and cyclic thermal treatment (D_{cyclic}) have been used to reconstruct the PAG using EDAX's OIM Analysis® v8.6 software. These samples were chosen based on the time between the start of cooling and the beginning of pearlite formation which can also play a role in PAG growth. For example, samples with slow cooling are subjected to temperatures above the pearlite formation during cooling for approximately 50 min at 0.1 °Cs^{-1} and 4 min at 1 °Cs^{-1}. This can lead to PAG growth due to prolonged time at high temperatures. On the other hand, samples subjected to intermediate cooling are assumed to have PAG equal to the ones of quenched samples as they are exposed to high temperatures for a short period during cooling.

As the reconstruction of PAG is only possible from martensite, additional interrupted heat treatments were done for slow-cooling samples. These heat treatments consisted of heating the samples with 200 °Cs^{-1} up to 900 °C with and without soaking for 5 min, followed by slow cooling (0.1 ° Cs^{-1} and 1 °Cs^{-1}) to 710 °C and subsequent quenching to get a final martensitic microstructure. The temperature choice was based on the dilatometry curves for slow cooling, as will be discussed in Section 3.3. The temperature of 710 °C is right before the decomposition of austenite into ferrite and pearlite in all cases, which gives a good estimation of the PAG development in the cooling stage.

The PAG reconstruction has been performed according to the Nishiyama-Wasserman orientation relationships between martensite and parent austenite grains. Fig. 5 shows the reconstructed PAG for samples D_{quench}, D_{cyclic}, S_{quench} and $S_{0.1}$. As can be seen, grains with an elongated shape are observed in samples with smaller PAG size (D_{quench} and D_{cyclic}). On the contrary, soaking at high temperatures leads to not only an increase on PAG size but also grains with a polygonal morphology. This is expected as the structure tends to reduce its internal energy by reduction of the grain boundary area. Table 2 presents the average reconstructured PAG size for each sample using N-W orientation relationship. Samples D_{quench} and D_{cyclic} show a similar average PAG of around 6 μm which is considerably smaller than for the other analysed samples. The smaller grains are attributed to the short time for grain growth as each heating–cooling cycle takes approximately 9 s. The similarities between these two samples also suggest that 10 cycles do not provide further grain refinement of the PAG.

On the other hand, a significantly higher PAG size is obtained for samples subjected to soaking and/or prolonged cooling stages. This increase is observed also for the width of the grain size distribution suggesting a bimodal distribution of PAG size. An additional observation is that the 5 min soaking time is sufficient for reaching a maximum growth of PAG. This is supported by the fact that $S_{0.1}$, exposed to high temperature for an extended period of time after soaking, has PAG size similar to S_{quench}.

Table 2
Quantification of the PAG size distribution.

Sample	Prior-austenite grain size (μm)	Distribution width (μm)
$D_{0.1}$	28.1	15.1
D_1	20.8	11.9
D_{quench}	6.4	3.7
D_{cyclic}	6.5	3.3
$S_{0.1}$	29.2	12.4
S_1	35.4	21.2
S_{quench}	34.6	17.6

3.3. Slow cooling (0.1 and 1 ° Cs^{-1})

Fig. 6a presents the change in length as a function of temperature for heat treatments D (direct cooling) and S (soaking) during cooling with cooling rates of 0.1 and 1 °Cs^{-1}. These curves allow the detection of phase transformations which are characterized by a change in slope of the dilatometry curve with respect to the FCC contraction curve (dotted gray line). The XRD results show that these cooling rates lead to a mix of BCC iron plus cementite, similar to the as-received material (89% BCC + 11% Cementite), see Table 3.

During slow cooling, a transformation is observed in the temperature range of 575 to 675 °C. The analysis of the dilatation curves suggests a two-step transformation with difference in the kinetics of the transformation, see Fig. 6b. At first, the pro-eutectoid ferrite starts forming at the prior-austenite grain boundaries at 680 °C for 0.1 °Cs^{-1} and at 660 °C for 1 °Cs^{-1}. The remaining austenite then transforms into pearlite from 650 °C and 610 °C for 0.1 °Cs^{-1} and 1 °Cs^{-1}, respectively. The SEM microscopy (Fig. 7) confirms the microstructure to be predominantly pearlitic, with presence of pro-eutectoid ferrite at the grain boundaries of the prior austenite. Samples with cooling rate of 0.1 °Cs^{-1} ($D_{0.1}$ and $S_{0.1}$) show regions of partial or complete spheroidization of the cementite lamellae, see Fig. 7. This spheroidization occurs as a consequence of prolonged cooling times after pearlite formation which allow cementite to reconfigure into a more stable morphology aiming at reducing the interfacial energy of the system [25].

At the cooling rate of 1 °Cs^{-1}, the delay of the start of pearlite formation causes an increase of pro-eutectoid ferrite fraction decorating the austenite grain boundaries when comparing to the sample cooled at 0.1 °Cs^{-1}. Due to the smaller austenite grain size of D samples than S samples, pro-eutectoid ferrite fraction is expected to be higher in the former. Unlike the samples subjected to 0.1 °Cs^{-1}, no cementite spheroidization is observed in these two treatments which is related to the lack of time during cooling for the cementite to reach a morphology with lower energy.

Cooling rates of 1 °Cs^{-1} lead to the formation of more pro-eutectoid ferrite when compared to the samples subjected to 0.1 °Cs^{-1}, see Fig. 6b, which can be explained by the difference in the

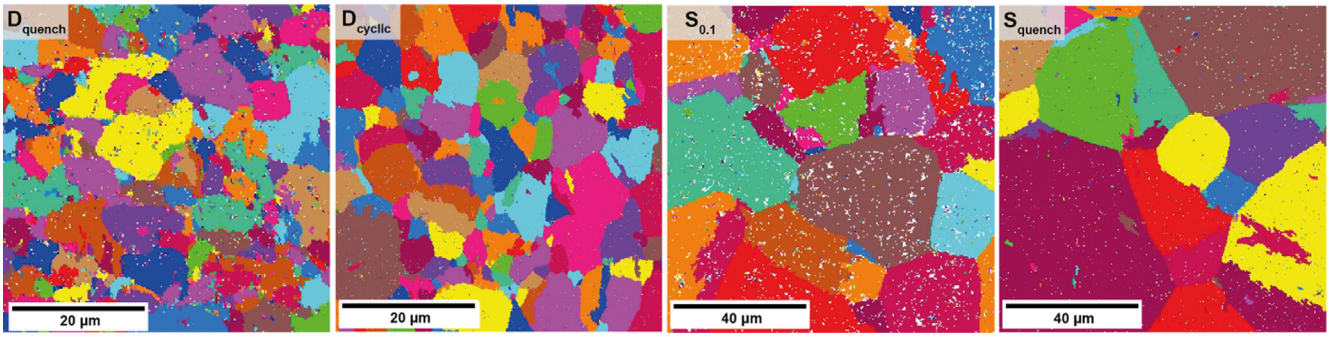

Fig. 5. Color coded unique grain color maps representing the reconstruction of PAGs from martensite variants according to Nishiyama-Wasserman (N-W) orientation relationship of samples D_{quench}, D_{cyclic}, S_{quench} and $S_{0.1}$ using EDAX v8.3 software.

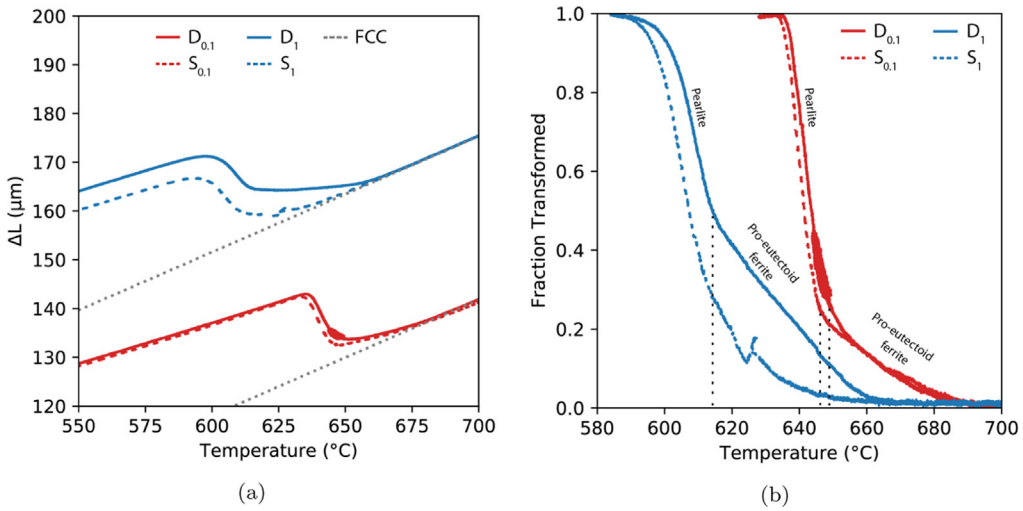

Fig. 6. (a) Change in length as a function of temperature obtained during cooling in dilatometry tests for specimens subjected to both heat treatments (D - solid line and S - dashed line) with low cooling rates (0.1 °Cs^{-1} - red and 1 °Cs^{-1} - blue) together with theoretical FCC expansion curves used to calculate the phase fractions. (b) Transformation products fractions calculated for each cooling rate.

Table 3
Phase fractions obtained via XRD for samples subjected to heat treatments D (direct cooling) and S (with soaking) with 0.1 and 1 ° Cs^{-1}.

Structure	Phase Fraction ± 1 (%)			
	$D_{0.1}$	$S_{0.1}$	D_1	S_1
BCC	90	91	92	91
Cementite	10	9	8	9
FCC	-	-	-	-

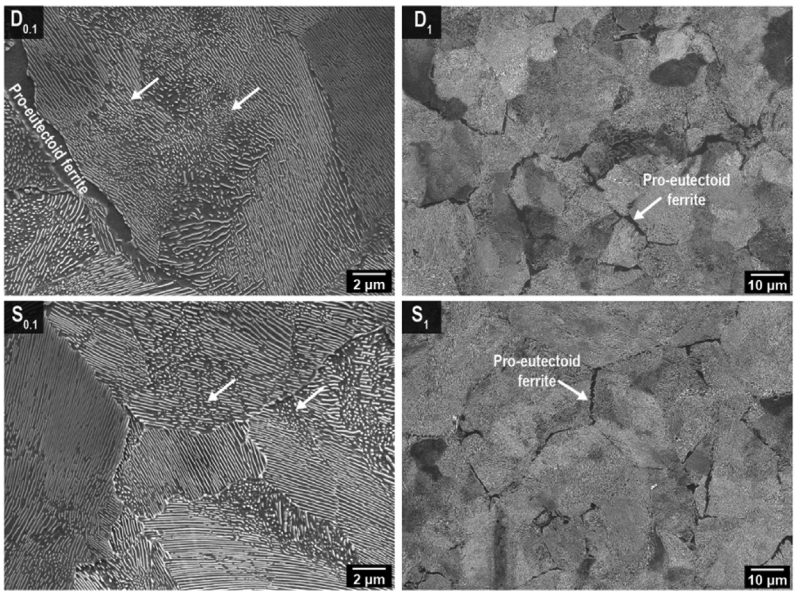

Fig. 7. SEM images showing the differences between direct cooling (D-samples) and soaking (S-samples) for low cooling rates. Two different magnifications are used for 0.1 and 1 °Cs^{-1} samples to highlight the pearlite spheroidization in the former and the pre-eutectoid ferrite size and morphology in the latter.

PAG size. When cooled with very low cooling rates, such as 0.1 °Cs^{-1}, the material is exposed to high temperatures for an extended period of time, resulting in larger PAG and lower nucleation site density for pro-eutectoid ferrite nucleation. As a result, less pro-eutectoid ferrite is present in the final microstructure, which is also observed in Fig. 6b.

The pro-eutectoid fraction was obtained via SEM image analysis using ImageJ software for samples with cooling rate of 1 °Cs^{-1}. The pro-eutectoid fraction is higher in sample D_1 (3.5 ± 0.5%) than in sample S_1 (2.2 ± 0.3%). Not only does sample D_1 have a higher fraction of pro-eutectoid ferrite, but also its morphology differs from S_1, see Fig. 7. While a relatively coarse pro-eutectoid ferrite is pre-

sent for specimen D_1, a distinctly refined morphology is achieved after soaking for 5 min.

3.4. Intermediate cooling (10 ° Cs^{-1})

A different behaviour is observed when the material is cooled with 10 ° Cs^{-1}. The deviation from linearity occurs in both D and S samples at about 650 °C, indicating the start of austenite decomposition, which progresses in three stages irrespective of soaking, as shown in Fig. 8. The first stage takes place between 550 and 650 °C and it is related with the pearlite formation. The pearlite formation does not account for two steps of transformation, as observed for samples with slow cooling, implying the absence or only a very small fraction of pro-eutectoid ferrite. The second stage is between 550 and 350 ° C, corresponding to bainite formation. The last stage, where the remaining austenite transforms into martensite, is at temperatures below 250 °C. However, this transformation is not completed and a small fraction of retained austenite remains in the final microstructure, see Table 4. The main difference between the two samples lies in the fractions of the microstructural constituents. A lower fraction of pearlite and bainite and consequently a higher fraction of martensite is seen (from the dilatometry curve analysis) to be present in the final microstructure of S_{10} when compared with D_{10}. After the heat treatment the analysis of the microstructure was performed using Optical Microscopy (OM) to investigate the homogeneity of the phases in low magnification. Fig. 9 shows the OM images of samples D_{10} and S_{10}, together with high magnification SEM images of specific regions. The microstructure consists of a mixture of martensite, bainite, pearlite and retained austenite. These microstructural constituents, however, are not distributed uniformly, but in alternating bands of bainite/pearlite (OM dark contrast) and martensite (OM white contrast). SEM micrographs allow better analysis of the microstructure of the dark-contrast regions which consist of a mix of bainite and pearlite. As expected from the transformed fraction curve, sample D_{10} contains a higher fraction of pearlite/bainite bands while sample S_{10} has a higher fraction of martensitic bands.

Fig. 10 displays the EPMA results for samples D_{10} and S_{10} which was done to determine the segregation of the elements in the bands. The measurement was performed along a line of approximately 700 μm located in the vicinity of thermocouple TC1. Although these experiments were carried out aiming at detection of C, Mn, Si and Cr, no segregation of C and Cr was observed. On the other hand, one can see that in both cases, martensitic regions (white contrast) account for positive segregation of Mn and Si, while pearlitic/bainitic regions (dark contrast) are locations of negative segregation of these elements.

Table 4
Phase fractions obtained via XRD for samples subjected to heat treatments D (direct cooling) and S (with soaking) with 10 °Cs^{-1}.

Structure	Phase Fraction ± 1 (%)	
	D_{10}	S_{10}
BCC	87	93
Cementite	4	5
FCC	9	2

3.5. Fast cooling (Quench)

For the fast cooling experiments, the actual cooling rates were measured in the temperature range of 800 °C and 500 °C after the heat treatment was performed. The approximate cooling rates for samples D_{quench} and S_{quench} are 347 °Cs^{-1} and 365 °Cs^{-1}, respectively. During fast cooling, no phase transformation takes place at higher temperatures, see Fig. 11a. According to the dilatometry curves, a final martensitic microstructure with a small fraction of retained austenite is formed. XRD measurements show that a similar content of retained austenite is obtained for both samples: 11% for D_{quench} and 9% for S_{quench}, with no cementite detected. Fig. 12 depicts the SEM micrographs of quenched samples. As expected, the initial pearlite, after transformation to austenite at high temperature, is completely transformed into martensite with a small fraction of retained austenite. Furthermore, regions of the so-called "ghost pearlite" are present inside martensitic areas in sample D_{quench} as indicated by a white arrow in Fig. 12. Those features have been previously reported in the literature [26–29] as a result of high Mn concentration in austenite regions formed from cementite dissolution. In absence of soaking at high temperature and due to the high heating rate, Mn, present in high concentration in the cementite lamellae, does not have time to homogenise in austenite

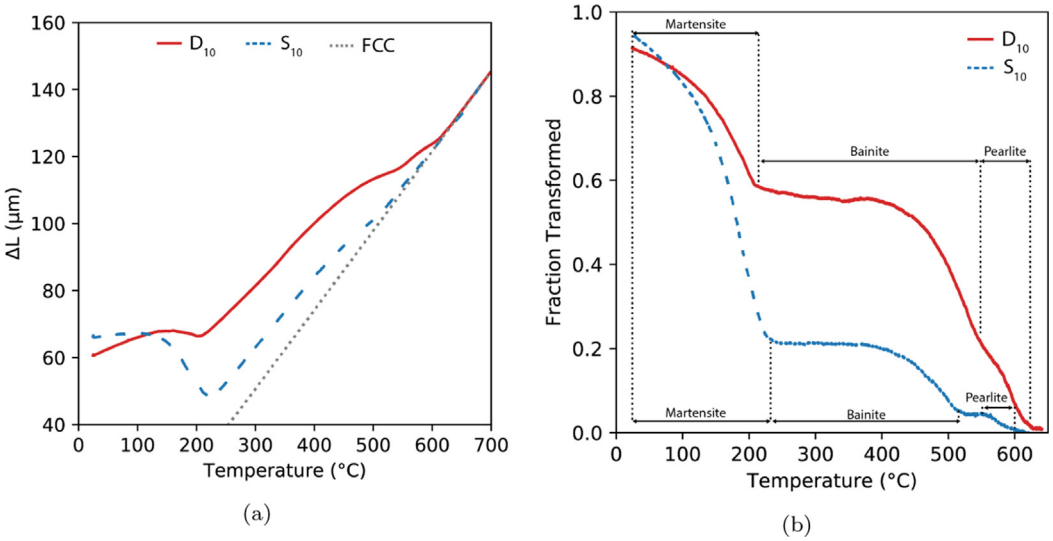

Fig. 8. (a) Change in length as a function of temperature curves obtained during cooling in dilatometry tests for specimens subjected to both heat treatments (D - solid line and S - dashed line) with intermediate cooling (10 °Cs^{-1}) together with theoretical FCC expansion curves used to calculate the transformed fractions. (b) Fractions of the microstructural constituents calculated for each sample.

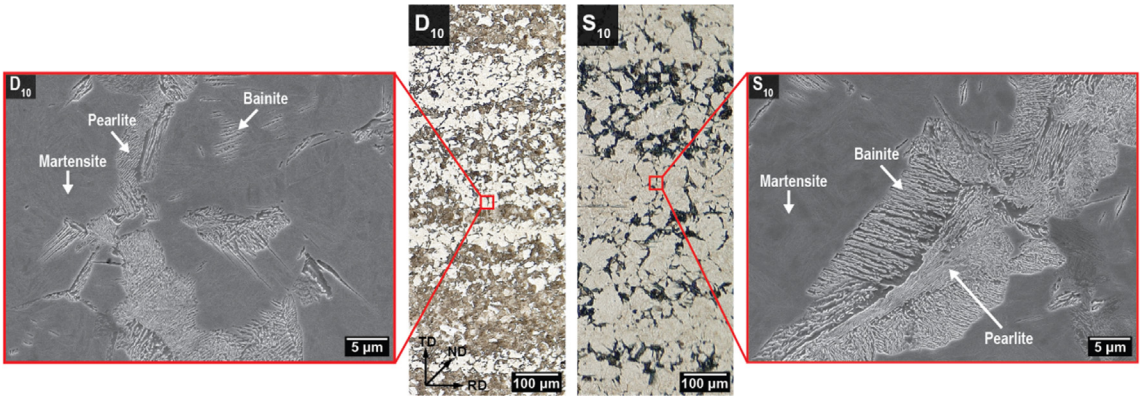

Fig. 9. OM and SEM images of samples D_{10} and S_{10} revealing the banded structure composed of martensite (white contrast) and a mix of bainite and pearlite (dark contrast). The orientation is defined as: RD - rolling direction, ND - normal direction (perpendicular to rail surface) and TD - transverse direction.

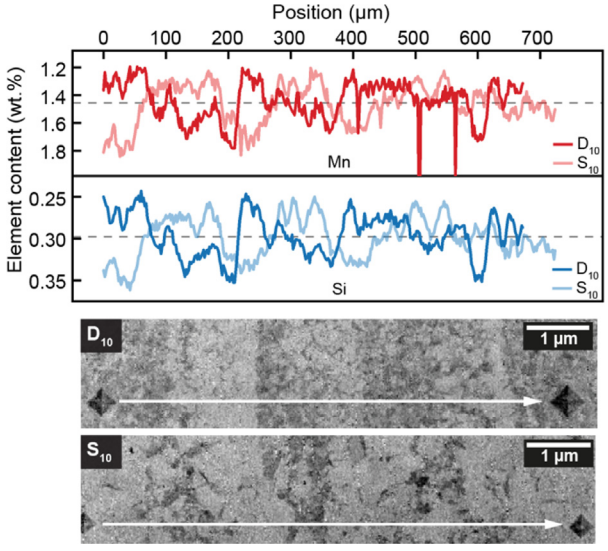

Fig. 10. EPMA analysis of D_{10} and S_{10} showing Mn (red) and Si (blue) distribution along the banded structure.

after cementite dissolution. Martensite containing a high Mn concentration is etched differently, thus revealing what is called "ghost pearlite". On the other hand, the soaking for 5 min at high temperatures can allow the diffusion of Mn out of cementite regions and its homogenisation in austenite, leading to absence of ghost pearlite, as observed in sample S_{quench}. This hypothesis is supported by calculating the diffusion distance of Mn in austenite after 5 min at 900 °C, which is expressed as

$$\lambda_{Mn} = \sqrt{2D^{\gamma}_{Mn}t} \tag{1}$$

where λ_{Mn} is the diffusion distance of Mn in austenite, t the diffusion time (5 min) and D^{γ}_{Mn} the diffusivity of Mn in austenite at 900 ° C (3.8×10^{-17} m^2s^{-1}). The latter is calculated using an activation energy (Q) of 246420 J/mol and deriving the pre-exponential factor ($D_0 = 3.69 \times 10^{-6}$ m^2s^{-1}) from data obtained with Thermo-Calc software. The diffusion distance is approximately 152 nm, which is in the same order of magnitude as the interlamellar spacing in pearlite. This supports the theory that under these circumstances, Mn has sufficient time to diffuse and homogenize in austenite, and hence no ghost pearlite is found in soaked samples.

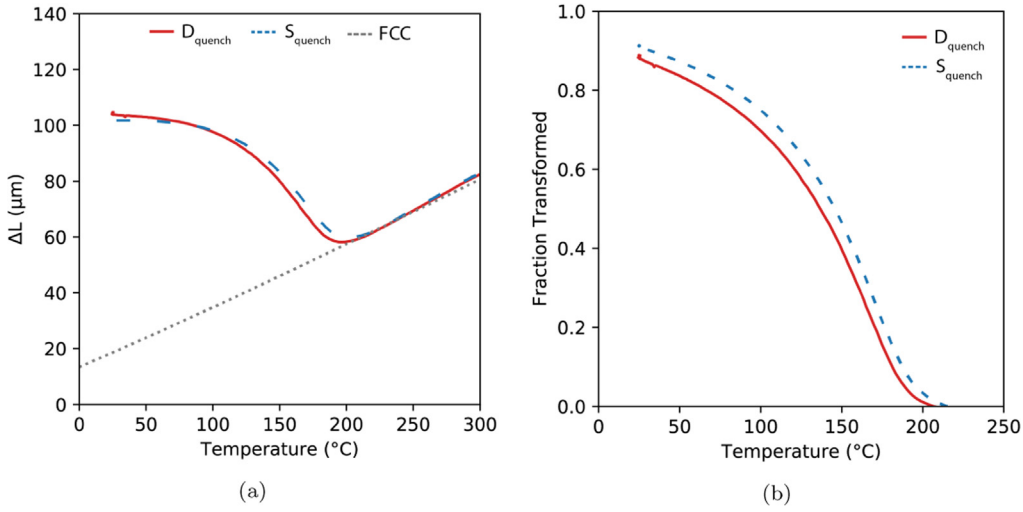

Fig. 11. (a) Change in length as a function of temperature curves obtained during dilatometry tests for specimens subjected to both heat treatments (D - red solid line and S - blue dashed line) with high cooling rates together with theoretical FCC expansion curves used to calculate the phase fractions. (b) Phase fraction calculated for each condition.

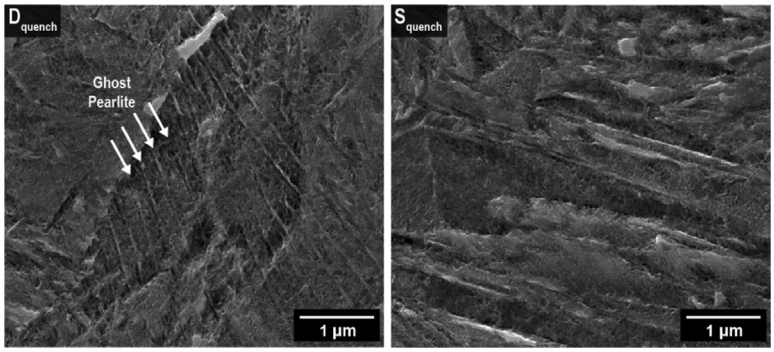

Fig. 12. SEM images showing the differences between direct cooling (D-samples) and soaking (S-samples) for quenched samples. Ghost pearlite is indicated with white arrows.

3.6. Cyclic heating and cooling

In this section the effect of cyclic heating and quenching will be discussed. The experiment aims at simulating the fast heating and cooling of the rail surface during several wheel passages under controlled laboratory conditions. Fig. 13a shows the cooling stage of dilatometry curves obtained for each cycle. As can be seen, in each cycle the main phase transformation is the martensite formation, which starts at approximately 300 °C.

Both heating and cooling stages of the dilatometry curve show a shift towards lower dilatation at each cycle, indicating an axial contraction of the sample. The same behaviour has been previously observed in the literature [30]. The authors ascribed the sample contraction during multiple thermal cycles to chemical segregation bands parallel to the sample axis. In the study, artificially banded samples (Mn segregation) were analysed and the axial strain obtained during cyclic heating was associated not only with the segregation of elements in the banded structure but also with the orientation of the sample with respect to the bands. In order to understand whether the shifts observed in D_{cyclic} are related with the anisotropy of the sample, the same heat treatment was imposed on a sample cut transversely to the rolling direction of rails. In this case, not only the shifts were much smaller but they would also decrease with each cycle, confirming a relation between the dilatometric shifts and anisotropic behavior of the sample. In order to capture detailed features, the scale at which the curves are depicted is greatly enlarged by subtracting the contribution of thermal expansion and contraction by calculating the length effects due to microstructural processes (L_m) according to

$$L_m = \delta L - (\lambda_i + \alpha T) \quad (2)$$

in which δL is the original dilatation signal. The slope α was chosen for both heating (0.10 μmK^{-1}) and cooling (0.22 μmK^{-1}) to optimise the scale. The parameter λ_i is chosen for each cycle i to achieve maximum coincidence of curves.

The resulting curves are exposed in Fig. 13b and c. As can be observed, the choice for λ_i aims at coinciding the curves in the austenite formation region in the case of heating stage and during martensite formation during cooling. During heating, the first cycle diverges from the subsequent ones, which is expected as the initial microstructure differs (pearlite for the first cycle and martensite in all subsequent cycles). Apart from the peak caused by temperature gradient (see Section 3.1), a change in the slope of the dilatation curve during the first portion of heating before austenite starts forming is also present, see Fig. 13b. It is observed that heating of an initial pearlitic structure accounts for a higher slope than the heating of martensite during the second and subsequent cycles. The change in slope is related with the initial microstructure (pearlite or martensite) and the variation of its thermal expansion, which is in agreement with the theoretical thermal expansion curves based on [31–33]. Besides that, a slight increase of the tempering effect with the number of cycles is also observed.

The cooling curves are very well reproducible apart from a slight deviation from the linearity (expansion) at high temperatures for the first cycle, see Fig. 13c. From the second cooling cycle onwards, there is a delay in the inset of this deviation to around 800 °C. At this temperature, austenite becomes unstable (Fig. 2) and possible precipitation of small fractions of ferrite or carbides can occur. However, in Section 3.5, sample D_{quench} (1 cycle) did not show the presence of ferrite nor carbides when observed in SEM or XRD measurements. Additionally, XRD measurements performed after 10 cycles reveal a total of 92% of BCC and 8% of FCC with no cementite detected. Besides, all cycles show a similar martensite-start temperature which confirms that no major differences are observed during the cooling portion of the cyclic heat treatment. Further investigation is necessary to understand the exact cause of this deviation whether it is due to ferrite or cabide precipitation or an instrumental artifact.

An interesting factor is that all curves are very well reproducible from the second cooling cycle onwards while deviations are observed in the first heating and cooling cycle and the second heating cycle. One possible explanation is related with the decomposition of austenite and element partitioning, specially Mn, which does not occur with only one cycle. A second explanation can be the carbide morphology that can also vary from the first and subsequent cycles.

3.7. Microhardness

Fig. 14 provides the Vickers microhardness values for each condition analysed in this work. No significant difference in hardness from the as-received material is observed in samples $D_{0.1}$ and $S_{0.1}$. This confirms that cooling at a rate of 0.1 °Cs^{-1} only leads to cementite spheroidization in some pearlite colonies. On the other hand, not only is there an increase in hardness for specimens cooled with 1 °Cs^{-1} when compared with 0.1 °Cs^{-1}, but the hardness of sample S_1 (339 HV) is slightly higher than that of sample D_1 (319 HV). This difference in hardness is explained by the decreased pro-eutectoid ferrite fraction after soaking which is related with the larger PAG size as discussed in Section 3.3.

A clear difference in hardness is observed between bands in the structure of samples cooled with 10 °Cs^{-1}. As expected, the martensitic bands have a greater hardness than the combination of pearlite and bainite, regardless of the soaking. In addition, the martensitic band formed after soaking presents a much higher hardness than the one found in sample D_{10}. The higher standard deviation of the hardness of D_{10} might be related with the smaller grains of martensite and higher fraction of pearlite and bainite that

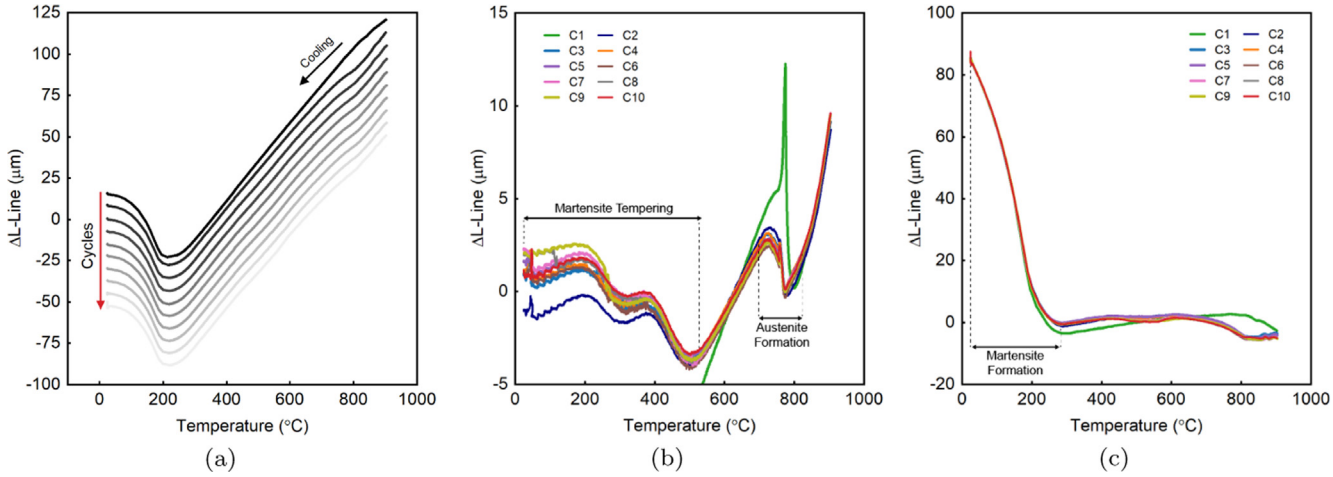

Fig. 13. (a) Cooling portion of dilatometry curves for specimen subjected to cyclic heating and quenching. (b) Optimized heating portion of dilatometry curves not considering the axial contraction of the sample. (c) Optimized cooling portion of dilatometry curves not considering the axial contraction of the sample.

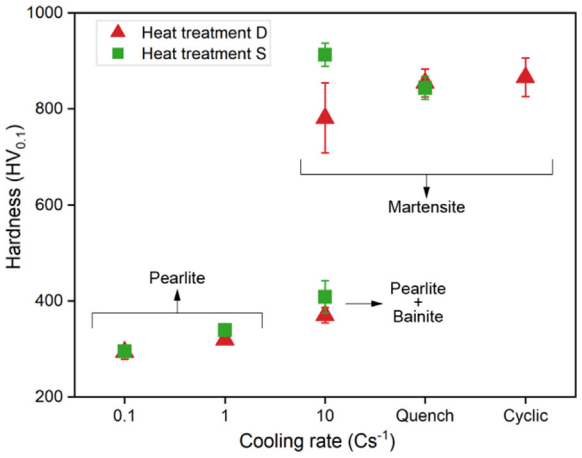

Fig. 14. Vickers microhardness measurements of samples subjected to heat treatments D and S. Two distinct measurements are presented for samples with cooling rates of 10 °Cs^{-1} in order to differentiate the mechanical response of the banded structure.

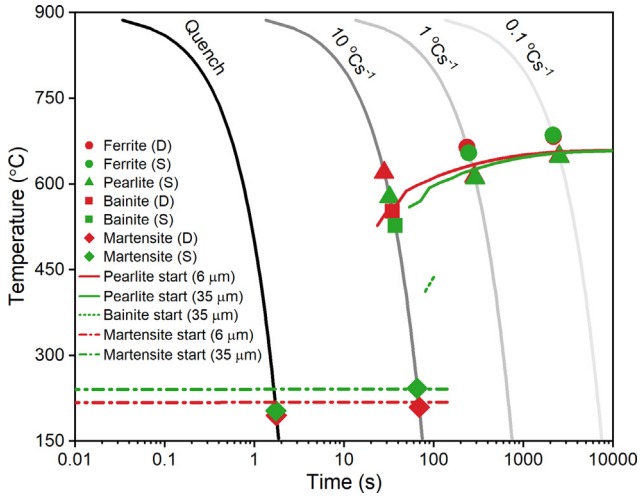

Fig. 15. Continuous Cooling Transformation diagram obtained via Thermo-Calc software and experimentally. The calculated CCT diagram (dashed lines) considers two initial PAG sizes: 6 μm (red) and 35 μm (green). The experimental CCT (symbols) exposes the starting temperatures of the different transformations formed after heat treatments D (red) and S (green).

can influence the local hardness. Quenching leads to martensitic structures with hardness of approximately 850 HV, which is lower than the hardness observed for the martensitic band of sample S_{10} but higher than sample D_{10}. Finally, the cyclic fast heating and quenching presents similar hardness as samples subjected to one cycle.

The higher hardness obtained for sample S_{10} could be caused by carbon enrichment of martensitic bands. However, both samples cooled at 10 °Cs^{-1} show similar martensite-start temperature, implying that strong differences in carbon content are not present. Furthermore, the enrichment of Mn and Si on martensitic bands reported in Section 3.4 is insufficient to affect the martensite-start temperature and, as a result, the hardness of martensite significantly.

3.8. CCT diagram

Fig. 15 shows the Continuous Cooling Transformation (CCT) diagram for R260Mn steel with two initial PAG sizes (6 μm and 35 μm) simulated with Thermo-Calc software together with the CCT diagrams obtained via analysis of the dilatometry curves. As discussed in Section 3.2, the initial PAG size is smaller for samples subjected to heat treatment D followed by fast cooling (D_{quench} and D_{10}). This leads to faster kinetics of ferrite and pearlite formation due to a higher density of nucleation sites for these microstructural constituents.

The PAG effect is not evident for very low cooling rates (0.1 and 1 °Cs^{-1}), explained by the prolonged time at high temperatures during cooling which allow similar PAG growth as seen in soaked samples. On the other hand, when cooling with 10 °Cs^{-1}, a delay is observed at the start of pearlite and bainite transformations for sample S_{10}, which is related to the lower nucleation-site density due to larger PAG. Although the simulated CCT diagram does not account for the presence of ferrite, the start temperature of pearlite transformation is consistent with the experiments.

For intermediate cooling rates, the bainitic transformation occurs for both direct-cooling and soaking samples, whereas it is expected to happen only for larger PAG in the simulated CCT diagram. Furthermore, the bainite start transformation temperatures are higher than expected from simulations. The transformation actually takes place at temperatures closer to the pearlite-start temperature. The simulation considers a homogeneous material,

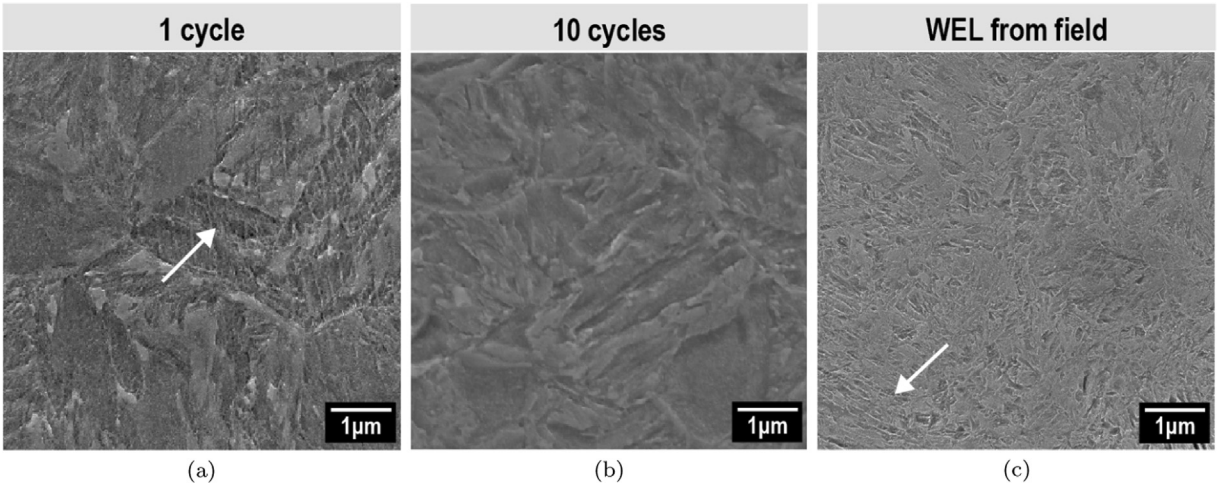

Fig. 16. SEM images of samples subjected to (a) 1 cycle (D_{quench}), (b) 10 cycles and (c) field WEL from a R260Mn steel. White arrows indicate the regions where ghost pearlite was observed.

however, segregation bands are observed while cooling at 10 °Cs^{-1}. These bands have a slightly different content of Mn and Si which can affect the bainite-start temperature.

The martensitic transformation starts first for S samples with respect to D samples in both the simulated and the experimental CCT diagram. In this case, the refinement of PAG results in lower martensite-start temperatures as previously mentioned in the literature [34,35].

3.9. Comparison with WEL from field

This section compares the microstructures acquired in controlled laboratory conditions to the WEL formed during wheel/rail contact in field conditions. A detailed analysis of the WEL from a field R260Mn sample used in this work can be found in the literature [14]. For the comparison, two laboratory samples were chosen: one subjected to fast heating followed by immediate quenching (D_{quench}) and one subjected to cyclic heating and quenching. These samples are thought to be a suitable depiction of the thermal cycle suggested by one of the WEL formation theories: rapid heating of the rail surface due to wheel contact, followed by quick cooling.

Fig. 16 presents the SEM micrographs of each sample. As previously mentioned, sample D_{quench} has a martensitic microstructure with some retained austenite. The same is observed after 10 cycles of fast heating and quenching, Fig. 16b. However, ghost pearlite (indicated with white arrow in Fig. 16a) is not present after cyclic heating and quenching. That indicates that Mn is able to diffuse out of the cementite lamella regions, homogenising in the martensitic microstructure. On the other hand, the WEL obtained from field R260Mn steel, Fig. 16c, shows the presence of similar features resembling the ghost pearlite. Previous atom probe tomography measurements confirmed Mn-rich zones inside of the WEL [14,18]. This means that even after several wheel/rail contacts, Mn does not have enough time to diffuse out of prior cementite regions and homogeneize in the austenite. This leads to Mn-rich locations which are etched differently than the matrix, showing the above mentioned, "ghost pearlite". However, according to the literature, the grain size of these regions is substantially lower (112 nm - 2 μm) than the grain size produced in the laboratory (6 μm). This is attributed to the fact that the laboratory experiments focused on creating WEL by imposing certain thermal cycles, but without mechanical loading. As a result, further grain refinement due to severe plastic deformation of the rail surface is not obtained in the experiments. On the other hand, the hardness of laboratory (850 HV) and field WEL (820 HV) are in a good agreement.

According to the comparison of these microstructures, the sample with a single cycle of fast heating and quenching has a microstructure that is more comparable to the one found in WEL from the field than the sample with 10 cycles. However, it is worth noting that in the experiments reported in this paper, complete austenitization of the rail surface followed by quenching to room temperature is simulated. During wheel/rail contact, austenitisation may not be complete. Certain contacts, for example, may reach intercritical temperature ranges and not cool down to room temperature before the next cycle begins. Furthermore, WEL is known to be formed in specific locations after a certain loading history of the rails which suggests that the rail surface is not fully austenitized in each wheel/rail contact. This means that it is unlikely that each rail/wheel contact reaches temperatures above A_3, leading to the full austenitization of the surface layer, as simulated in the present paper. The peak temperature in the contact patch might reach temperatures within the intercritical temperature range and only a fraction of the pearlite is transformed into austenite and thus, martensite after quenching. All these variations might have an impact on the final WEL microstructure.

4. Conclusions

This paper discusses the microstructural changes observed in a pearlitic railway steel subjected to fast heating (200 °Cs^{-1}) followed by controlled cooling at different cooling rates. The effect of severe plastic deformation is not taken into account. The experimental investigation shows that:

- As a result of the intermediate cooling rates, martensitic bands and pearlitic/bainitic bands are observed in the microstructure. This unforeseen behavior is caused by the segregation of elements such as Mn and Si. The segregation bands promote microstructural anisotropy, which causes a shift in the dilatometer curves during cyclic heat treatments.
- Soaking for 5 min at high temperatures allows sufficient Mn diffusion in austenite to eliminate traces of prior cementite.
- Cyclic heating to the fully austenitic range and quenching does not lead to continued grain refinement of prior-austenite grains, indicating that the main cause of grain refinement in the WEL is the plastic deformation of railway surfaces during wheel and rail contact.

- Comparable hardness is obtained for WEL produced in laboratory and the one from field conditions. This suggests that phase transformation is a dominant aspect in WEL formation and increase in hardness of these layers.
- Repeated cycling leads to a microstructure which is more homogeneous than the one observed after one cycle. This is mainly due to the absence of ghost pearlite after 10 cycles suggesting that Mn is able to diffuse out of cementite lamellae locations, homogenising in the austenite. However, in field conditions the rail experiences possible variations in peak temperature, heating rate and cooling rate which have an effect on the final microstructure of the surface layer.
- Similar microstructural features are observed in WEL from field and after a single cycle of fast heating followed by quenching. However, the very small grain size observed in WEL produced during wheel/rail contact is not reproducible by thermal heating only. This suggests that such level of grain refinement is due to severe plastic deformation.

Declaration of Competing Interest

The authors declare that they have no known competing financial interests or personal relationships that could have appeared to influence the work reported in this paper.

Acknowledgment

This research was carried out under project number S16042a in the framework of the Partnership Program of the Materials innovation institute M2i (www.m2i.nl) and the Technology Foundation TTW (www.stw.nl), which is part of the Netherlands Organization for Scientific Research (www.nwo.nl). The authors would like to thank ProRail for its financial support and DekraRail for arranging specimens for this research. Ruud Hendrikx at the Department of Materials Science and Engineering of the Delft University of Technology is acknowledged for the X-ray analysis. Tuan Nguyen Minh is aknowledged for supporting in the prior-austenite grain reconstruction.

References

[1] J.E. Garnham, C.L. Davis, Rail materials, in: R. Lewis, U. Olofsson (Eds.), Wheel-rail interface handbook, Woodhead Publishing Limited, 2009, pp. 125–171.
[2] M. Ghodrati, M. Ahmadian, R. Mirzaeifar, Modeling of rolling contact fatigue in rails at the microstructural level, Wear 406–407 (2018) 205–217.
[3] N. Larijani, J. Brouzoulis, M. Schilke, M. Ekh, The effect of anisotropy on crack propagation in pearlitic rail steel, Wear 314 (1–2) (2014) 57–68.
[4] L. Wang, A. Pyzalla, W. Stadlbauer, E.A. Werner, Microstructure features on rolling surfaces of railway rails subjected to heavy loading, Mater. Sci. Eng., A 359 (1–2) (2003) 31–43.
[5] J.W. Ringsberg, A. Bergkvist, On propagation of short rolling contact fatigue cracks, Fatigue Fract. Eng. Mater. Struct. 26 (2003) 969–983.
[6] P. Clayton, D. Danks, Effect of interlamellar spacing on the wear resistance of eutectoid steels under rolling-sliding conditions, Wear 135 (1990) 369–389.
[7] P. Clayton, D.N. Hill, Rolling contact fatigue of rail steel, Wear 117 (1987) 319–334.
[8] J. Takahashi, Atom probe study on microstructure change in severely deformed pearlitic steels: Application to rail surfaces and drawn wires, IOP Conference Series: Materials Science and Engineering 219 (1) (2017).
[9] H.W. Zhang, S. Ohsaki, S. Mitao, M. Ohnuma, K. Hono, Microstructural investigation of white etching layer on pearlite steel rail, Mater. Sci. Eng., A 421 (1–2) (2006) 191–199.
[10] M. Steenbergen, R. Dollevoet, On the mechanism of squat formation on train rails - Part I: Origination, Int. J. Fatigue 47 (2013) 361–372.
[11] G. Baumann, H.J. Fecht, S. Liebelt, Formation of white-etching layers on rail treads, Wear 191 (1–2) (1996) 133–140.
[12] W. Lojkowski, M. Djahanbakhsh, G. Bürkle, S. Gierlotka, W. Zielinski, H.J. Fecht, Nanostructure formation on the surface of railway tracks, Mater. Sci. Eng., A 303 (1–2) (2001) 197–208.
[13] J. Wu, R.H. Petrov, M. Naeimi, Z. Li, R. Dollevoet, J. Sietsma, Laboratory simulation of martensite formation of white etching layer in rail steel, Int. J. Fatigue 91 (2016) 11–20.
[14] J. Wu, R. Petrov, S. Kölling, P. Koenraad, L. Malet, S. Godet, J. Sietsma, Micro and Nanoscale Characterization of Complex Multilayer-Structured White Etching Layer in Rails, Metals 8 (10) (2018) 749.
[15] W. Osterle, H. Rooch, A. Pyzalla, L. Wang, Investigation of white etching layers on rails by optical microscopy, electron microscopy, X-ray and synchrotron X-ray diffraction, Mater. Sci. Eng., A 303 (2001) 150–157.
[16] A. Kumar, G. Agarwal, R. Petrov, S. Goto, J. Sietsma, M. Herbig, Microstructural evolution of white and brown etching layers in pearlitic rail steels, Acta Mater. 171 (2019) 48–64.
[17] Q. Lian, H. Zhu, G. Deng, X. Wang, H. Li, X. Wang, Z. Liu, Evolution of thermally induced white etching layer at rail surface during multiple wheel/train passages, Int. J. Fatigue 159 (July 2021) (2022) 106799.
[18] J. Takahashi, K. Kawakami, M. Ueda, Atom probe tomography analysis of the white etching layer in a rail track surface, Acta Mater. 58 (10) (2010) 3602–3612.
[19] A. Kumar, G. Agarwal, R. Petrov, S. Goto, J. Sietsma, M. Herbig, Microstructural evolution of white and brown etching layers in pearlitic rail steels, Acta Mater. 171 (2019) 48–64.
[20] S.M.C. van Bohemen, The nonlinear lattice expansion of iron alloys in the range 100–1600 K, Scripta Mater. 69 (4) (2013) 315–318.
[21] M. Jung, S.J. Lee, Y.K. Lee, Microstructural and dilatational changes during tempering and tempering kinetics in martensitic medium-carbon steel, Metall. Mater. Trans. A 40 (3) (2009) 551–559.
[22] J. Hidalgo, M.J. Santofimia, Effect of Prior Austenite Grain Size Refinement by Thermal Cycling on the Microstructural Features of As-Quenched Lath Martensite, Metall. Mater. Trans. A 47 (11) (2016) 5288–5301.
[23] B. Ravi Kumar, B. Mahato, S. Sharma, J.K. Sahu, Effect of cyclic thermal process on ultrafine grain formation in AISI 304L austenitic stainless steel, Metall. Mater. Trans. A 40 (13) (2009) 3226–3234.
[24] L. Duan, J. Wang, Q. Liu, X. Sun, J. Cao, Austenite Grain Growth Behavior of X80 Pipeline Steel in Heating Process, J. Iron. Steel Res. Int. 17 (3) (2010) 62–66.
[25] Víctor Alcántara Alza, Spheroidizing in Steels: Processes, Mechanisms, Kinetic and Microstructure - A Review, IOSR Journal of Mechanical and Civil Engineering 18 (3) (2021) 63–81.
[26] W.W. Sun, Y.X. Wu, S.C. Yang, C.R. Hutchinson, Advanced high strength steel (AHSS) development through chemical patterning of austenite, Scripta Mater. 146 (2018) 60–63.
[27] J.L. Cunningham, D.J. Medlin, G. Krauss, Effects of induction hardening and prior cold work on a microalloyed medium carbon steel, J. Mater. Eng. Perform. 8 (4) (1999) 401–408.
[28] S. Li, Z.N. Yang, M. Enomoto, Z.G. Yang, Study of partition to non-partition transition of austenite growth along pearlite lamellae in near-eutectoid Fe-C-Mn alloy, Acta Mater. 177 (2019) 198–208.
[29] Z.D. Li, G. Miyamoto, Z.G. Yang, T. Furuhara, Kinetics of reverse transformation from pearlite to austenite in an Fe-0.6 mass pct C alloy and the effects of alloying elements, Metall. Mater. Trans. A 42 (6) (2011) 1586–1596.
[30] R.A. Jaramillo, M.T. Lusk, M.C. Mataya, Dimensional anisotropy during phase transformations in a chemically banded 5140 steel, Part I: Experimental investigation. Acta Materialia 52 (4) (2004) 851–858.
[31] S.J. Lee, M.T. Lusk, Y.K. Lee, Conversional model of transformation strain to phase fraction in low alloy steels, Acta Mater. 55 (3) (2007) 875–882.
[32] R.K. Dutta, R.M. Huizenga, M. Amirthalingam, A. King, H. Gao, M.J.M. Hermans, J. Sietsma, I.M. Richardson, In-situ synchrotron diffraction studies on transformation strain development in a high strength quenched and tempered structural steel - Part I. Bainitic transformation, Metall. Mater. Trans. A 45 (1) (2014) 218–229.
[33] L. Cheng, A. Böttger, Th.H. de Keijser, E.J. Mittemeijer, Lattice parameters of iron-carbon and iron-nitrogen, Scripta metallurgica et materialia 24 (2) (1990) 509–514.
[34] H.S. Yang, H.K.D.H. Bhadeshia, Austenite grain size and the martensite-start temperature, Scripta Mater. 60 (7) (2009) 493–495.
[35] S.J. Lee, Y. Kook Lee, Effect of Austenite Grain Size on Martensitic Transformation of a Low Alloy Steel, Mater. Sci. Forum 475–479 (2005) 3169–3172.